


Article

Multi-Source Information Monitoring Test of Fractured Rock Mass Destruction Characteristics and Sensitivity Analysis of Precursor Phenomena

Qinghe Zhang ^{1,2,*} , Tianle Zheng ^{2,*}, Xiaorui Wang ² and Zhiyuan Fang ²

¹ State Key Laboratory Mine Response and Disaster Prevention and Control in Deep Coal Mine, Anhui University of Science and Technology, Huainan 232001, China

² School of Civil Engineering and Architecture, Anhui University of Science and Technology, Huainan 232001, China; xiaorui06sherry@163.com (X.W.); zyfsdu@126.com (Z.F.)

* Correspondence: qhzhang@aust.edu.cn or zhangqhsdu@163.com (Q.Z.); tianlz2021@163.com (T.Z.)

Abstract: The accuracy of the monitoring information is particularly important for exploring fractured rock mass deformation and failure mechanisms and precursor characteristics. Appropriate monitoring methods can not only timely and effectively reflect the failure laws of fractured rock masses but also play an early warning role. To explore more reasonable monitoring methods, uniaxial compression experiments and real-time non-destructive monitoring on prefabricated fractured rock specimens through DIC, AE, and IRT were conducted; the strain field, temperature field, ringing frequency, standard deviation, etc. were analyzed; and correlation between the three methods in the information of audience was explored. The results show the following. (1) The failure evolution process of fractured rock mass can be divided into four stages. DIC can detect the initiation and propagation of cracks near the fractures of the specimen at the earliest stages. (2) The order of occurrence of precursor phenomena in multi-source monitoring information is different, which is vertical strain field > shear strain field > horizontal strain field > temperature field > ringing times. (3) The dispersion degree of standard deviation of each field is obviously different; the infrared temperature field is greater, but the strain field and temperature field show the same trend. (4) There are obvious precursors before the specimen is on the verge of instability; acoustic emission detected two consecutive increases in the cumulative number of ringing before destruction, which means the most obvious precursors. The research results can provide a theoretical basis for the precursory information capture and damage early warning of the fractured rock mass destruction process.

Keywords: fractured rock mass; digital image correlation; acoustic emission; infrared radiation temperature; multi-source monitoring; failure precursor



Citation: Zhang, Q.; Zheng, T.; Wang, X.; Fang, Z. Multi-Source Information Monitoring Test of Fractured Rock Mass Destruction Characteristics and Sensitivity Analysis of Precursor Phenomena. *Energies* **2022**, *15*, 538. <https://doi.org/10.3390/en15020538>

Academic Editors: Changkook Ryu, Hanpeng Wang and Bing Zhang

Received: 25 November 2021

Accepted: 5 January 2022

Published: 12 January 2022

Publisher's Note: MDPI stays neutral with regard to jurisdictional claims in published maps and institutional affiliations.



Copyright: © 2022 by the authors. Licensee MDPI, Basel, Switzerland. This article is an open access article distributed under the terms and conditions of the Creative Commons Attribution (CC BY) license (<https://creativecommons.org/licenses/by/4.0/>).

1. Introduction

Defects of different scales in the rock mass are one of the key factors affecting the stability of the rock mass [1,2]. Under construction disturbance, engineering rock defects may cause cracks to initiate, expand, slip, lose stability, and even cause serious geological disasters. According to the international climate protection agreement, coal mining will soon be drastically reduced. Nevertheless, it is undeniable that the safety of professional miners is paramount. Therefore, the deformation and failure monitoring of fractured rock masses is particularly important for the stability of engineering rock masses. Ke Zhang et al. conducted real-time, non-contact, and non-destructive tests of fractured sandstone specimens through digital image-related technology [3] Yan Du et al. introduced dynamic monitoring indicators to summarize the dynamic response during the failure process of rock and soil mass, and they concluded that the natural vibration frequency can provide data support for rock and soil damage [4]. Yan Du, Zhixiang Wu, et al. used laser Doppler vibration measurement technology to explore the precursor phenomena of rock separation

failure [5]. Existing studies have shown that during the loading process of fractured rock specimens, strain localization bands will be generated around the fractures, which are accompanied by acoustic emission and infrared radiation, and the signal responses of these physical quantities are closely related to the failure process of fractured rock masses. Zhigang Li et al. used SEM and acoustic emission systems to analyze the microscopic failure morphology of silty slate under different foliation angles and the corresponding acoustic emission characteristics during the deformation and failure process, thus revealing the deformation and failure mechanism of silty slate under different foliation angles [6]. Guokai Zhang et al. used stress–strain testing, high-speed camera combined with AE testing technology to study the strength and deformation characteristics of fractured rocks, analyzed the law of crack initiation, expansion, and coalescence, clarified the evolution difference of AE characteristics at different stages of crack growth, and revealed the influence of real-time crack propagation on rock strength and deformation characteristics [7]. Quan Lou et al. used infrared radiation temperature measurement technology to study the failure mechanism of rocks [8]. For this reason, predecessors used Digital Image Correlation (DIC), Acoustic Emission (AE), or Infrared Radiation Temperature (IRT) to monitor the signal response law during the destruction of fractured rock specimens.

DIC is a non-contact optical measurement method that effectively measures the strain localization zone. DIC calculates the global strain field information by scanning the displacement of the scattered spots in the area. This emerging technology overcomes the limitations of traditional contact strain gauges for measuring one-point strain. In recent years, the role of DIC technology in related engineering technology fields has become more and more obvious. Yuan et al. [9] used the DIC method to quantitatively analyze the evolution of the crack displacement field during the fracture process of the rock mass, and based on the change law of the normal and tangential displacement fields of the crack surface, they proposed the fracture type of the filled fractured rock mass. Deepanshu Shirole et al. [10] quantitatively evaluated the tensile and shear damage areas of rock mass based on the full-field strain information, and they found that the crack tip has relatively high tensile and shear damage. Yimin Song et al. [11] used DIC technology as a test. The monitoring method quantitatively studied the evolution characteristics of the strain field and the phenomenon of strain localization during the failure process of the intact marble specimen. Ke Zhang et al. [12] measured the evolution characteristics of the strain field in the fracture process of fractured sandstone, introduced the standard deviation of the strain field and the differentiation rate index, and put forward the precursor information of the fractured rock mass tension and shear crack initiation.

AE is a very effective micro-crack identification technology, which is very sensitive to measuring and identifying internal fractures in rock masses. Chuanxi Li et al. [13] used the bispectral analysis method to analyze the acoustic emission signals at different stages of rock mass loading, and they found that due to the different damage mechanisms, the number of peaks and peaks of the acoustic emission signal produced by the test beam are very different. Qibin Lin et al. [14], based on the AE technology, identified the crack coalescence law of rock mass effectively and divided the types of crack coalescence. Giuseppe Lacidogna et al. [15] used AE technology and DIC technology to dynamically monitor the fracture cracks of concrete beams and identified the cracks damage evolution process. Kongling Guo et al. [16] conducted fracture mechanics tests on rock materials with three-dimensional fractures under hydraulic coupling, and they believed that low-frequency signals continued to increase and high-frequency signals appeared suddenly and densely, which could be used as an early warning reference information for the overall rupture of the specimen.

IRT is a non-contact electromagnetic monitoring technology that can monitor the temperature changes of infrared radiation on the rock surface in real time. Xianzhen Wu, Chunlai Wang, and others studied the characteristics of the instantaneous change of the infrared temperature field during the rock mass fracture process, and they found that there is a good corresponding relationship between the temperature field and the stress field

of the loaded rock sample, and the abnormal temperature turning point can be used as the key prediction point of rock mass failure [17,18]. Kewang Cao et al. [19] studied the infrared radiation temperature characteristics during the expansion of rock mass, and they found that the infrared radiation temperature change is approximately linearly related to the volumetric strain increment. Rongxi Shen et al. [20] analyzed the infrared radiation temperature characteristics in the process of rock mass expansion and found that the temperature change of infrared radiation is approximately linearly related to the increase in volumetric strain. Xiaoming Sun et al. [21] found that the appearance and expansion of macro cracks during the explosion process resulted in obvious spatial differentiation of the infrared radiation temperature on the surface of the rock mass, and this anomaly was regarded as an important precursor before the occurrence of rockburst.

The above research focuses on monitoring the information of a single physical signal such as strain field, infrared radiation temperature field, or acoustic emission during the failure process of the specimen. In fact, in the process of rock destruction and evolution, various signals with different precursors and different energies may be generated. Moreover, the sensitivity and response laws of these physical signals also have certain differences. The real-time simultaneous monitoring of multi-source physical signals can well avoid the above-mentioned problems. At present, there are few studies on the multi-source monitoring information during the failure process of fractured rock specimens. The response law and precursor relationship of the multi-source monitoring information during the failure process of fractured rock specimens are still unclear. Therefore, this paper uses DIC, AE, and IRT—three non-destructive monitoring technologies—to simultaneously monitor the failure process of prefabricated fractured rock specimens, focusing on the corresponding relationship between strain field, acoustic emission signal, infrared radiation temperature field, and fracture process of fractured rock specimens and precursor sensitivity. The research results can provide a theoretical basis for the precursory information capture and damage early warning of the fractured rock mass destruction process.

2. Experimental Design

2.1. Experimental Materials and Test Pieces

It is difficult to make real fractured rock specimens [12]. In this paper, the cement mortar material with controllable material composition and properties is used to prefabricate the fractured specimens. The mechanical properties of this type of material are similar to typical sandstone, which can simulate the uniformity of the rock well [22,23]. The material mix ratio is ordinary Portland cement/sand/water = 1.00:2.34:0.35. The cuboid specimen was prepared by the pouring method, and the specimen size was 60 mm × 20 mm × 120 mm (length × width × height), as shown in Figure 1.

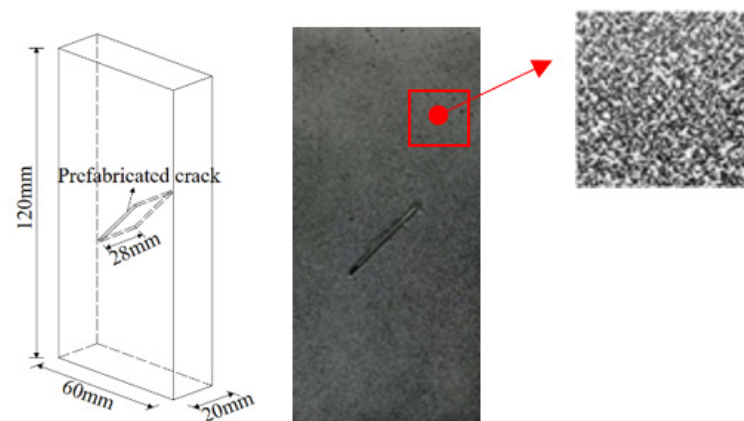


Figure 1. Test block model diagram.

Before pouring the test piece, a square slice with a length of 28 mm, a thickness of 1 mm, and the same width as the test piece was fixed in advance at the corresponding position of the mold to prefabricate the cracks with an inclination angle of 45° . After the specimen is initially set, take out the sheet, and then use an 8 mm syringe to slowly inject gypsum into the crack to form a weakly filled crack specimen. After the production is completed, put it in a standard curing room for curing. After the curing is completed, a white primer and black spots are sprayed on the surface of the test piece to form a uniform and clear artificial speckle so that the DIC equipment can capture and measure the strain of the whole field.

2.2. Experimental Device and Method

In order to obtain the response characteristics of multi-physical quantities in the fracture process of fractured rock mass, this paper constructs an integrated test system consisting of a loading unit, DIC unit, infrared radiation unit, and acoustic emission unit, as shown in Figure 2. Among them, the loading unit mainly includes a rigid servo testing machine, which can apply an axial displacement load to the specimen, and the loading rate is 0.005 mm/s. The DIC unit adopts the Vic-2D™ System, in which the industrial camera has a resolution of 2592×1944 pixels. The camera is aimed at the surface of the specimen sprayed with an artificial speckle field, and the acquisition frequency is 50 Hz. At the same time, in order to improve the accuracy of image collection, LED cold light sources are used to fill the test surface. The infrared radiation unit is an online thermal imaging system with a spatial resolution of 640×480 pixels, a temperature sensitivity of 0.02°C , and an imaging rate of 10 Hz. The acoustic emission unit adopts PCI-2 type acoustic emission monitoring equipment produced by American Physical Acoustics Company. The collection frequency response range is 50–400 kHz, and the sampling frequency is 1 MHz, in order to accurately collect the rupture signal of the specimen.

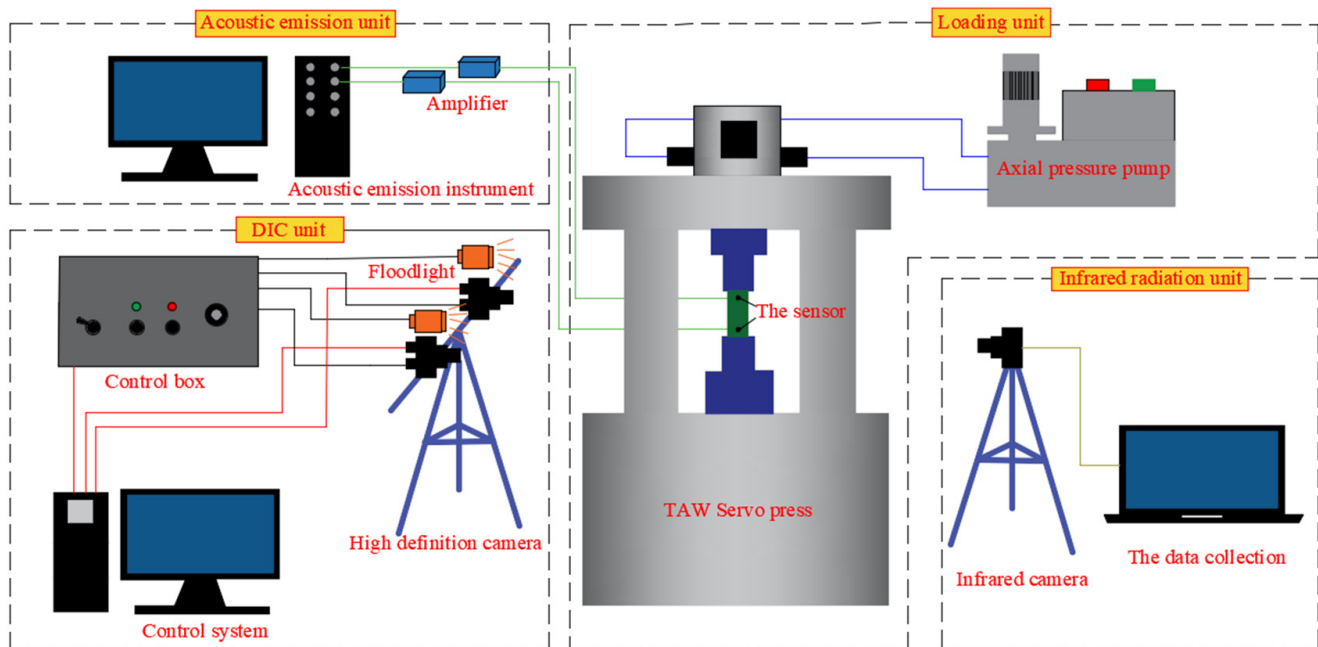


Figure 2. Test system.

The uniaxial compression test adopts a displacement loading control method with the loading rate is 0.005 mm/s. Industrial cameras, infrared thermal imaging cameras, and acoustic emission sensors are used for real-time monitoring. Industrial cameras and infrared thermal imaging cameras are installed on the front and back sides of the specimen, and the acoustic emission sensor is fixed on the side wall of the specimen. To maintain a

high degree of consistency with loading and monitoring equipment in time, internet time is used to correct the experimental time. At the same time, in order to ensure good contact between the specimen and the loading instrument, the Vaseline coupling agent was applied between the probe and the specimen. Finally, all the collection equipment is connected to the Internet for information collection.

3. Test Results

In order to avoid errors caused by the dispersion of the specimens, four specimens with the same material ratio and experimental conditions were subjected to uniaxial compression tests at room temperature. The stress–strain curve is shown in Figure 3. It can be seen from Figure 3 that the stress–strain evolution process of the four fractured specimens is basically similar. Due to space limitations, this article selects the failure process of the No. 2 specimen for analysis. In order to facilitate the comparison between the stress–strain curve and the test phenomenon, eight representative characteristic points are selected on the stress–strain curve of the No. 2 specimen. Among them, the characteristic points a–b are the pore compaction stage, the characteristic points b–e are the linear elastic stage, the characteristic points e–g are the nonlinear growth stage, the characteristic point g is the peak stress point, and the characteristic point h is the failure point. Figure 4 shows the crack growth corresponding to the characteristic points (a–h).

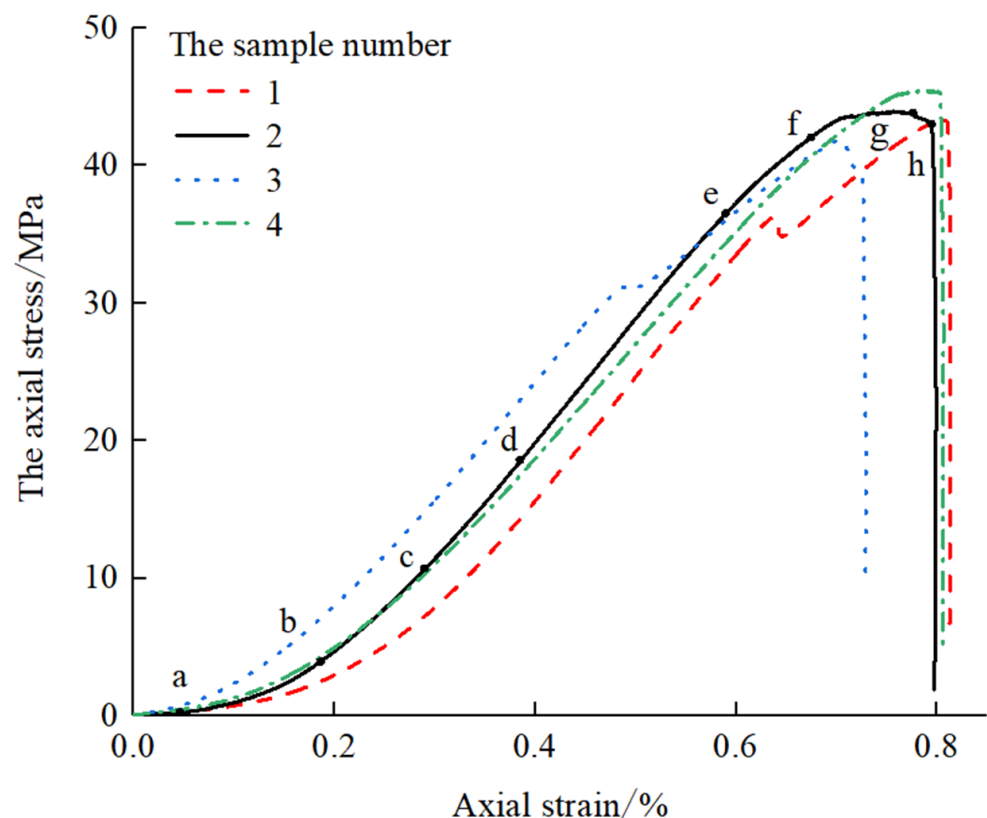


Figure 3. Stress–strain curve of fractured rock mass.

It can be seen from Figures 3 and 4 that the failure evolution process of the specimen is closely related to the crack propagation process. (1) In the pore compaction stage (characteristic points 3a,b), the stress–strain curve is relatively gentle, the internal pores of the fractured specimen are gradually compacted, and no new cracks are found near the fractures, as shown in Figure 4a,b. (2) In the elastic deformation stage (characteristic points 3b,e), the stress–strain curve is basically linear, the specimen is in an elastic compression state, and no new cracks are found near the cracks, as shown in Figure 4b–e. (3) In the non-linear

growth stage (characteristic points 3e–g), when the load reaches 81.43% of the peak stress, new cracks appear near the cracks, and the cracks extend to both ends of the specimen along the loading direction, they continue to load to 95.83% of the peak stress, and the cracks are loaded along the load. The direction accelerates to both ends, and when the stress reaches the peak, the new cracks are already very obvious (see Figure 4e–g). (4) In the post-peak stage (characteristic points 3g,h), after the stress reaches 100% of the peak stress, the crack propagates rapidly, and the crack penetrates the specimen at the characteristic point h. When the block penetration is approaching, the stress value is 97.21% of the peak stress, the stress–strain curve is a cliff-like drop, and the specimen undergoes brittle failure, as shown in Figure 4g,h.

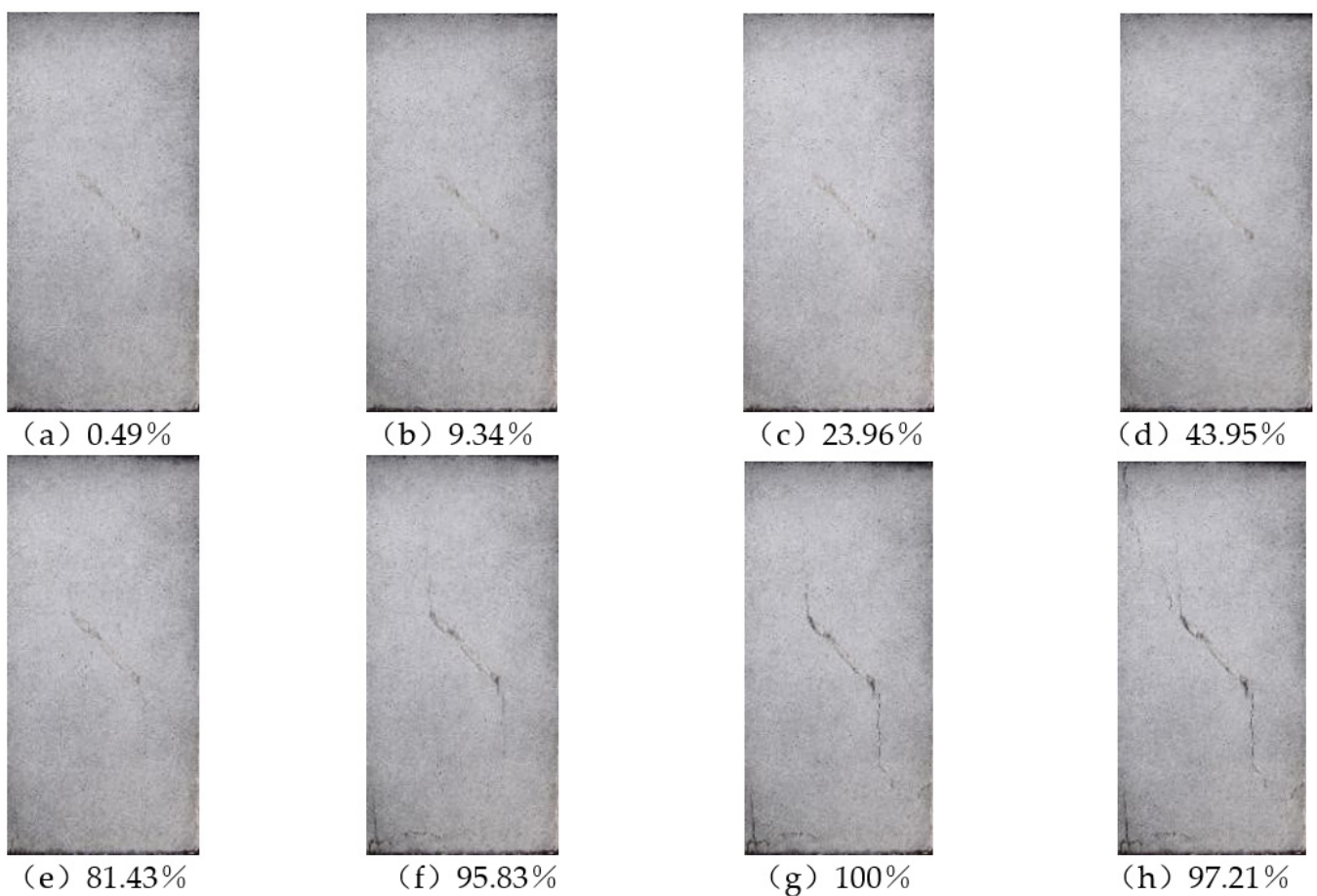


Figure 4. Crack propagation.

3.1. Strain Field Evolution Law

The DIC unit collected more than 8000 crack growth pictures. The digital image correlation software Vic-2D is used to process the speckle image to obtain the horizontal strain field, vertical strain field ε_{yy} and shear strain field γ_{xy} during the loading process of the fracture specimen. The strain field distribution at the eight characteristic points is shown in Figures 5–7.

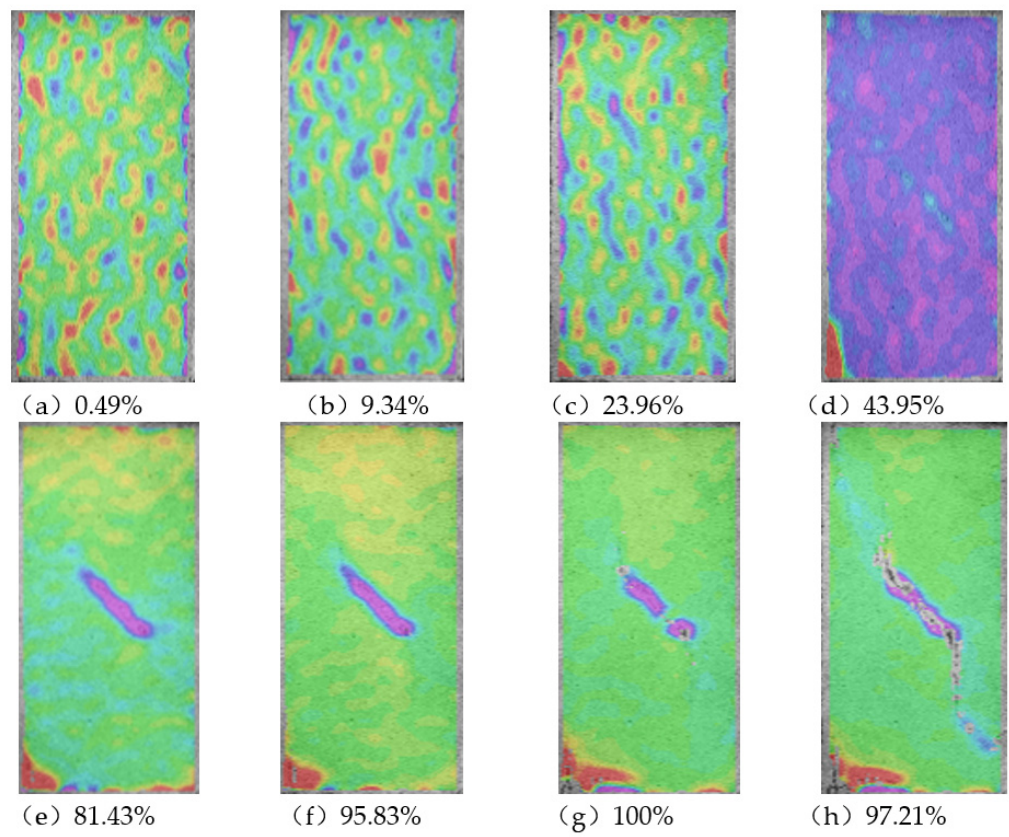


Figure 5. Horizontal strain field.

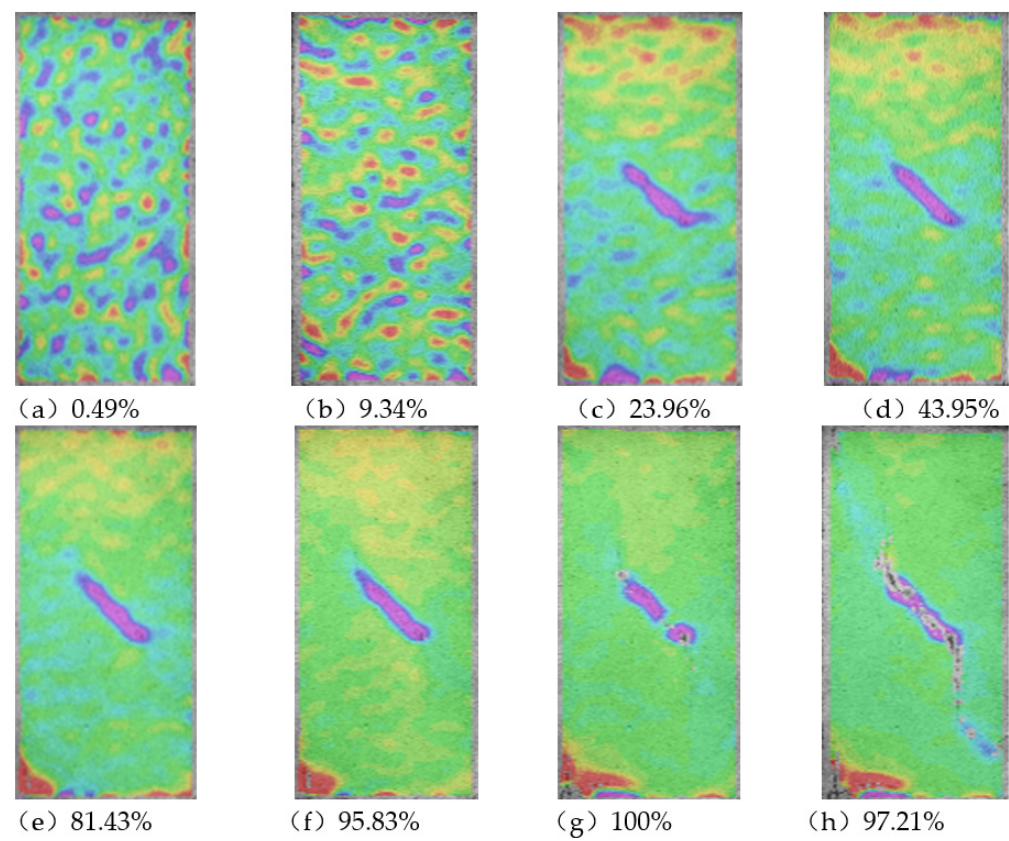


Figure 6. Vertical strain field.

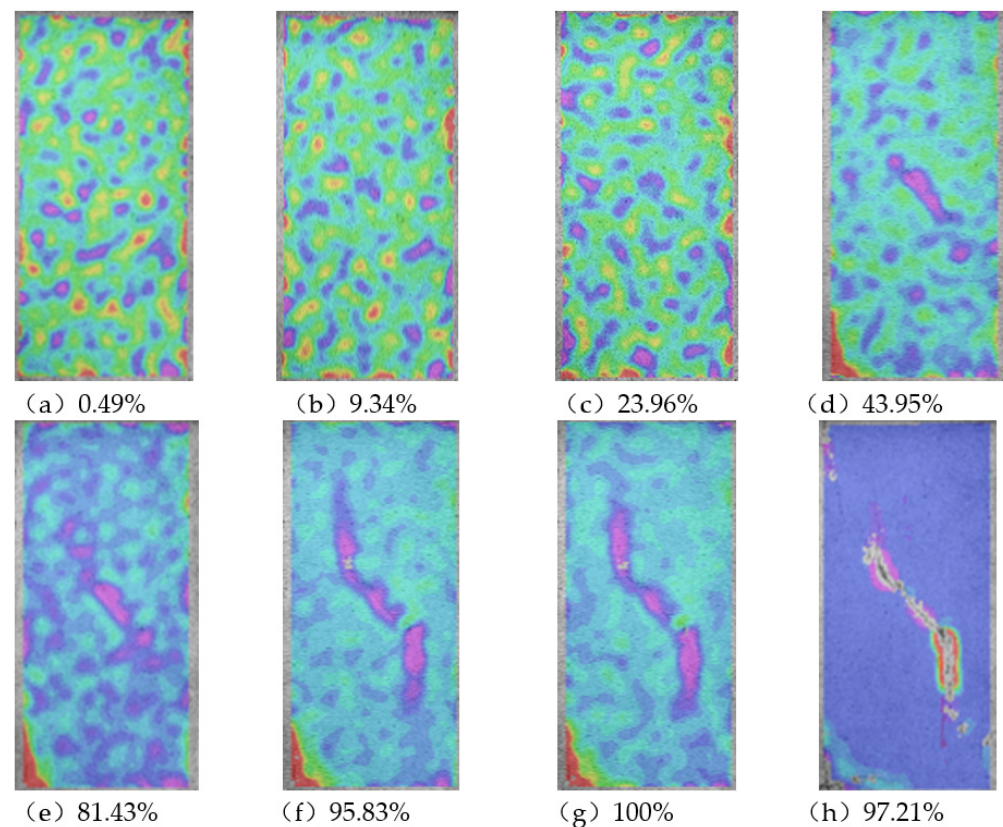


Figure 7. Shear strain field.

Comparing Figures 5–7 and Figure 4, it can be found that the strain field evolution of the specimen under uniaxial compression is closely related to crack propagation. The surface strain field of the specimen gradually changed from a uniform distribution to a strain-concentrated area covering the prefabricated crack. Subsequently, a strain localization zone was generated near the crack tip and continued to expand. In the pore compaction stage (characteristic points 4a,b), there is no obvious change in the three strain fields, as shown in Figure 5a,b, Figure 6a,b, and Figure 7a,b. In the elastic deformation stage (characteristic points 4b,e), it can be seen from Figure 4c,d that the specimen did not produce visible cracks, but strain localization bands appeared near the cracks in the three strain fields. Figure 5e, Figure 6c–e, and Figure 7d,e show that strain field monitoring has certain precursors; in the non-linear growth stage (characteristic points 4e,f), new generation appears near the cracks. For cracks, the strain localization range of the specimen is enlarged, and there is a tendency to expand, as shown in Figure 5e,f, Figure 6e,f, and Figure 7e,f. In the post-peak stage (characteristic point 4g,h), the strain localization zone accelerates and expands and penetrates to both ends of the specimen along the loading direction, as shown in Figure 5h, Figure 6h, and Figure 7h. Therefore, strain localization is an important feature of the instability failure of the specimen, which is manifested by the uneven distribution of local strain on the surface of the specimen, which indicates the initiation, propagation, and penetration path of macroscopic cracks.

3.2. Change Law of Temperature Field

Infrared thermal imaging cameras have collected more than 1600 infrared radiation thermal maps. The thermal distribution of infrared radiation temperature field at eight characteristic points is shown in Figure 8.

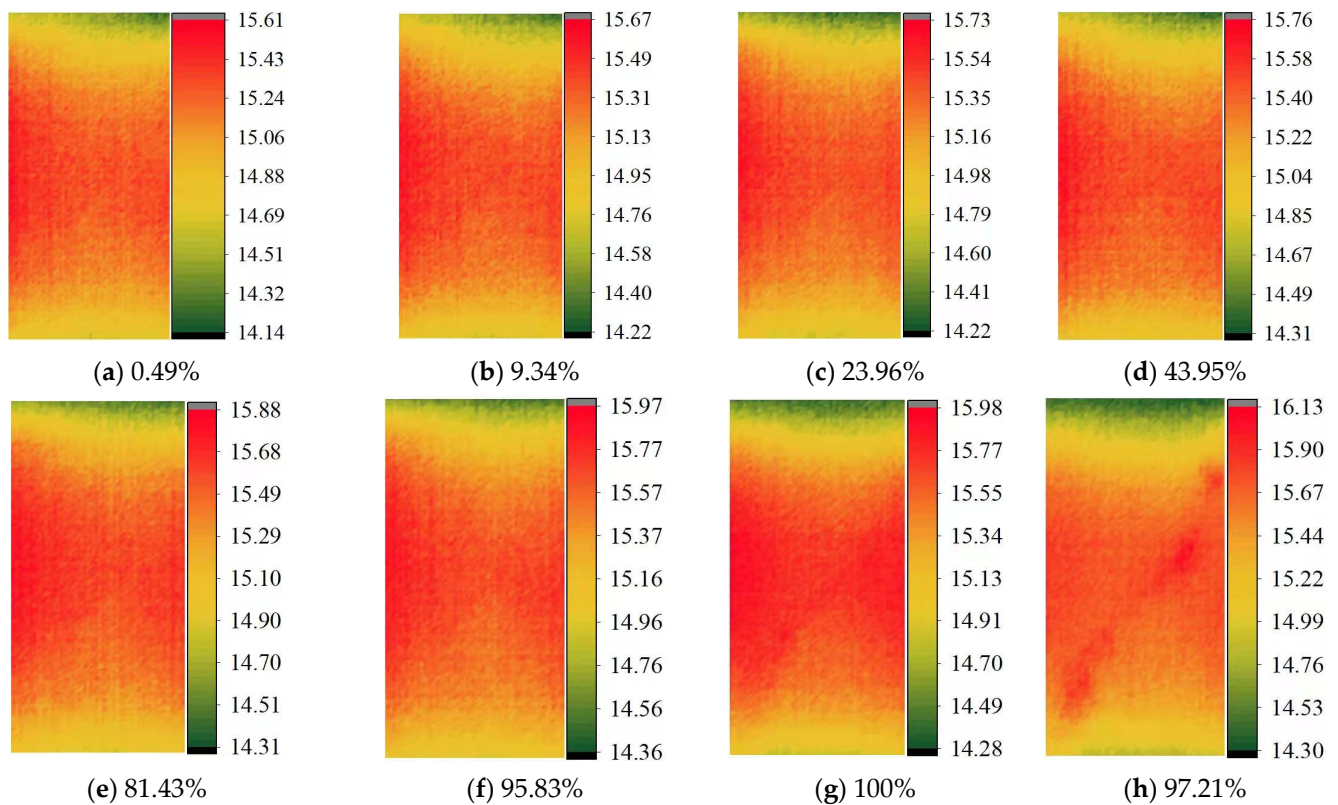


Figure 8. Infrared radiation temperature field (unit: °C).

Figure 8 shows that at different stages of deformation and failure of the specimen, there are certain differences in the evolution of the temperature field. Table 1 shows the highest temperature and lowest temperature difference of the temperature field from a to h. In Table 1, the highest temperature of the specimen at time a is 15.61 °C and the lowest temperature is 14.14 °C; the highest temperature of the specimen at time h is 16.13 °C, and the lowest temperature is 14.30 °C; the highest temperature increases by 0.53 °C, and the lowest temperature increases by 0.24 °C. The maximum temperature rise is more significant.

Table 1. The highest and lowest temperature statistics of the surface temperature of the specimen.

Feature Point	a	b	c	d	e	f	g	h	Temperature Difference
Highest temperature	15.61	15.67	15.73	15.76	15.88	15.97	15.98	16.13	0.53
Lowest temperature	14.14	14.22	14.22	14.31	14.31	14.36	14.28	14.30	0.24
Temperature difference	1.47	1.45	1.51	1.45	1.57	1.61	1.70	1.83	

Before the specimen is loaded to the non-linear growth stage (characteristic points a–e), the temperature change on the specimen surface is not obvious, the infrared radiation temperature field is relatively uniform, and the difference between the highest temperature and the lowest temperature is relatively stable; when the load reaches the peak under stress (characteristic point g), the temperature field rises obviously, and the temperature near the crack rises obviously, which indicates the accelerated growth of the crack; at the moment of failure of the test block (characteristic point h), obvious high-temperature bands appear on the infrared thermal imaging cloud image. The spatial position is basically the same as the fissure penetration position.

3.3. Evolution of Acoustic Emission

During the loading and rupture process of the specimen, the accumulative impact frequency curve of acoustic emission ringing presents the characteristics of phase changes, as shown in Figure 9.

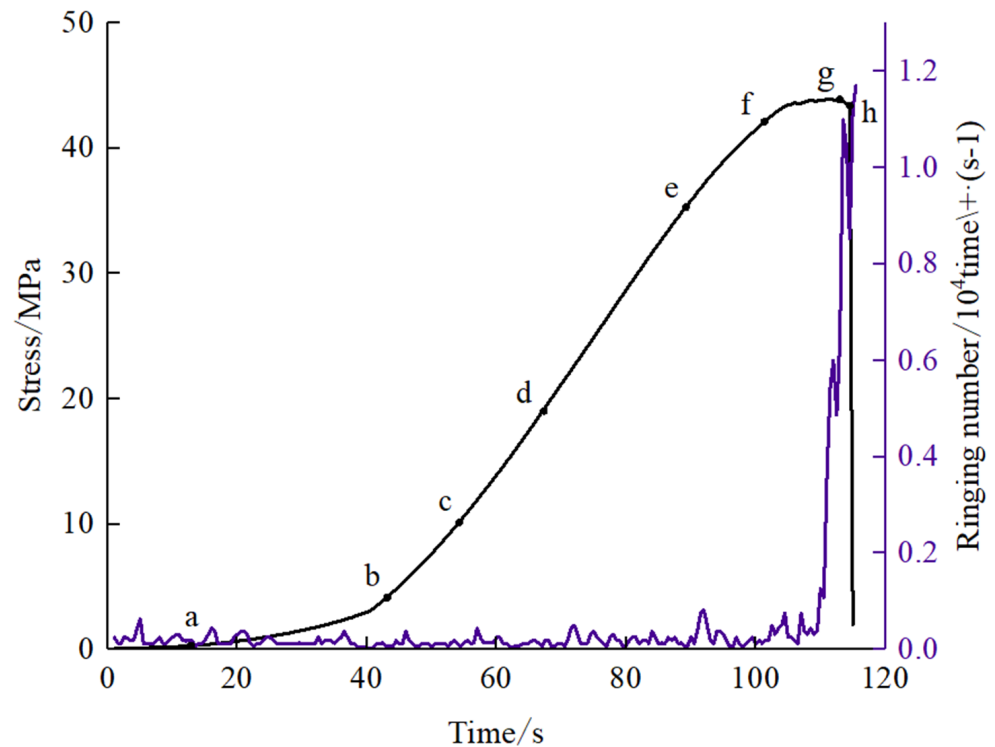


Figure 9. Ringing frequency–time relation curve.

Figure 9 shows that the number of acoustic emission ringing in the pore compaction stage and the elastic deformation stage of the specimen presents a small peak, and the ringing number changes relatively smoothly and fluctuates within a certain range. In the non-linear growth stage, the cumulative number of ringing impacts began to increase. Before the peak stress point g, the cumulative number of ringing impacts increased twice, and the first increase occurred during the accelerated crack propagation stage, indicating crack growth. Then, they speed up; the second rise occurs near the peak stress. After the peak stress, the accumulative number of ringing impacts increased again, and then, the specimen was destabilized and damaged. Therefore, the two increases in the number of ringing correspond to two important stages in the evolution of crack failure, and the rising point of the cumulative number of ringing impacts can be used as an obvious precursor point.

4. Result Analysis and Discussion

The fractured specimens have obvious precursors before they are on the verge of destruction. Guoqing Chen et al. proposed that the anomalous location of infrared thermal imaging is consistent with the future fracture area of the rock [24]. At the same time, Ke Zhang et al. proposed that strain localization bands will appear on the eve of rock mass failure [12]. Shuhong Wang and others used the improved acoustic emission equipment to adopt a relative positioning method to locate complex samples and engineering rock acoustic emission events [25]. Figures 5–7 show that during the loading process of the cracked specimen, the strain at the prefabricated crack is obviously concentrated, and the strain localization zone accelerates along the loading direction until it penetrates before the failure. The surface temperature of the specimen rises slowly as a whole, and obvious high-

temperature bands appear at the time of penetration (characteristic point h). Figure 9 shows that the acoustic emission monitoring of the cracked specimen is on the verge of penetration, and the cumulative number of ringing has risen twice in a row, and the precursor response is more obvious than the infrared radiation temperature and strain field. Under the monitoring of DIC, AE, and IRT, there is a big difference between the occurrence time of the damage and failure precursor phenomenon of the specimen, the strain field appears to have strain localization, the temperature field appears to have high-temperature bands, and the cumulative number of acoustic emission impacts increases. The time sequence of the occurrence of precursor phenomena is: Vertical strain field > Shear strain field > Horizontal strain field > Temperature field > Accumulated number of ringing impacts.

Judging from the failure history of the specimen, the failure duration of the specimen is about 120 s, of which the compaction stage (a,b) is about 43 s, the elastic deformation stage (b–d) is about 47 s, and the non-linear development stage (e,f) is about 27 s, while the post-peak stage (g,h) is only 2 s. In the recorded damage photos, no new cracks were found near the cracks of the specimen before time e. After time e, new cracks began to grow at both ends of the crack. Before continuing to load to the peak stress, the crack gradually expands. At the peak stress, the crack rapidly expands to the two ends of the specimen, and the total time of crack initiation and expansion is about 29 s.

In terms of monitoring information, during the failure process of the specimen, the surface strain field and infrared temperature field of the specimen gradually changed from a uniform distribution state to a strain concentration area covering the cracks and then the expansion and penetration of the strain concentration area. Therefore, the appearance of a strain localization zone and high-temperature zone is an important feature of fractured rock specimen failure. A direct comparison of strain field and temperature field will be more complicated; in order to better compare, we introduce a standard deviation calculation formula rather than a single statistical comparison so that the conclusions reached are both in line with practical needs and can greatly facilitate our calculations. In order to carry out statistical analysis on the evolution law of the variable field and infrared radiation temperature field, this paper introduces the “standard deviation” index to quantitatively describe the evolution law and degree of differentiation of the two field variables.

Standard deviation is one of the most frequently used statistical indicators in mathematical statistics. It reflects the degree of dispersion of data. The development of strain localization bands and high-temperature bands during the loading process will increase the degree of data differentiation. This index is introduced in this article. The standard deviation calculation methods of the three strain fields (ε_{xx} , ε_{yy} , ε_{zz}) are shown in Formulas (1) and (2).

$$S_{\varepsilon,i} = \sqrt{\frac{\sum_{j=1}^n (\varepsilon_{ij} - \bar{\varepsilon}_i)^2}{n-1}} \quad (1)$$

$$\bar{\varepsilon}_i = \frac{\sum_{j=1}^n \varepsilon_{ij}}{n} \quad (2)$$

where $S_{\varepsilon,i}$ is the sample standard deviation of the strain field at the i -th moment; n is the number of temperature field sub-zones; ε_{ij} is the horizontal strain of the j -th subregion at the i -th moment; and $\bar{\varepsilon}_i$ is the mean value of the strain field of the n sample sub-regions at the i -th moment.

In the same way, the sample standard deviation index is used to calculate the dispersion degree of the global temperature field of the specimen at each time, as shown in Formulas (3) and (4).

$$S_{T,i} = \sqrt{\frac{\sum_{j=1}^m (T_{ij} - \bar{T}_i)^2}{m-1}} \quad (3)$$

$$\bar{T}_i = \frac{\sum_{j=1}^m T_{ij}}{m} \quad (4)$$

where $S_{T,i}$ is the sample standard deviation of the temperature field at the i -th moment; m is the number of temperature field sub-zones; T_{ij} is the average temperature of the image source in the j -th subzone at the i -th moment; and \bar{T}_i is the mean value of the temperature field of the m sample sub-regions at the i -th moment.

The standard deviation curves of the horizontal strain field ε_{xx} , the vertical strain field ε_{yy} , the shear strain field γ_{xy} , and the infrared radiation temperature field of the specimen are shown in Figure 10.

It can be seen from Figure 10 that the standard deviation curve of the strain field and temperature field can be roughly divided into three stages. (1) Initial differentiation stage: In this stage, the standard deviation increases slowly, and the dispersion degree of the standard deviation of the strain field and the temperature field also begins to increase slowly. At this stage, the pores of the specimen are gradually compacted, and the differentiation of the strain field and the temperature field is not obvious. (2) The stable differentiation stage: The standard deviation of this stage increases stably, and the dispersion of the standard deviation of the strain field and the temperature field continues to increase. At this time, the test block is in the elastic deformation stage, a stable differentiation phenomenon occurs at this stage, the temperature field has a local heating phenomenon, and the strain field has a strain localization zone. (3) Accelerated differentiation phase: The standard deviation increases at this stage. The dispersion degree of the standard deviation of the strain field and the temperature field increases rapidly. High-temperature bands appear in the temperature field, and at the same time, the strain localization bands in the strain field accelerate and extend along the loading direction. At the same time, the test block is in the non-linear growth stage and the post-peak stage.

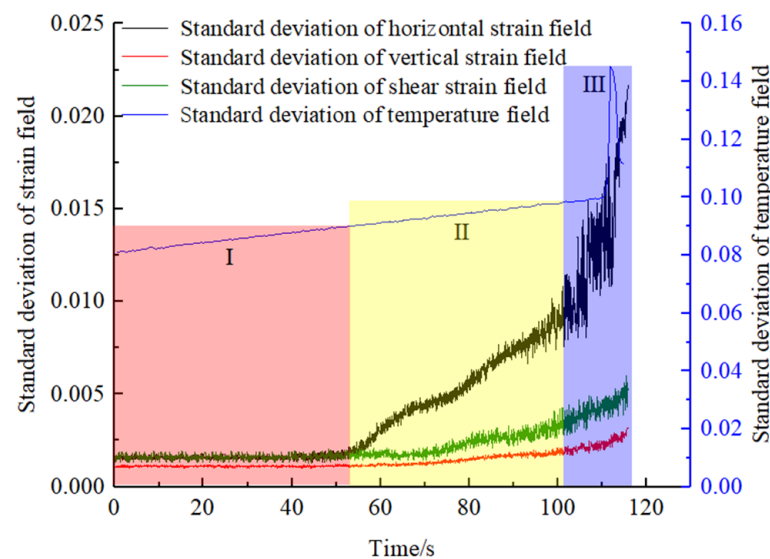


Figure 10. Standard deviation of axial strain field vs. time curve.

From the above analysis of the degree of dispersion of the corresponding variable field and temperature field, as time increases, the degree of dispersion of the standard deviation of the temperature field and the strain field changes to different degrees. After the pore compaction phase is over, the strain field and temperature field begin to differentiate, and the differentiation becomes more and more obvious with the progress of the experiment. The appearance of the differentiation indicates the propagation and evolution of cracks. Comparing the standard deviation of the strain field and the temperature field, it can be seen that the phenomenon of strain field divorce is earlier than the temperature field, which is consistent with the previous analysis. Before the specimen is on the verge of destruction, the standard deviation of the temperature field undergoes a significant mutation, and this mutation may be more easily observed.

5. Conclusions

- (1) From the perspective of the failure evolution process of the specimen, the strain localization zone in the three strain fields appeared earlier than the surface cracks of the specimen. Among them, the strain localization phenomenon appeared first in the vertical strain field, and the strain localization zone appeared until it penetrated. For the specimen, the duration of this stage accounts for about 2/3 of the entire process of the specimen's failure and evolution; it is more time-efficient than the infrared temperature field and the cumulative number of acoustic emissions to monitor the abnormal phenomenon of the fractured specimen.
- (2) The occurrence time of the precursor phenomenon is different during the loading process of the specimen. Among them, the first occurrence of strain localization is in the vertical strain field, and the sequence of precursor phenomena is: Vertical strain field > Shear strain field > Horizontal strain field > Temperature field > Accumulated number of ringing impacts.
- (3) With the failure of the specimen, the dispersion of the standard deviation of the strain field and the temperature field also increases, and the standard deviation of the temperature field and the standard deviation of the strain field show the same trend during the crack propagation process, and the standard deviation of the infrared radiation temperature field is greater than the standard deviation of the stress field. The degree of dispersion is greater, the differentiation phenomenon is more obvious, and the mutation of the differentiation phenomenon in the infrared temperature field is more obvious.
- (4) The fractured specimen has a precursory reaction before it is on the verge of destruction. Before the specimen is on the verge of failure, the strain localization zone in the strain field accelerates and penetrates to the two ends of the specimen, and the high-temperature strip is captured in the infrared temperature field. At the same moment, the cumulative number of impacts of acoustic emission ringing rises twice, and the precursor is the most obvious response.

This paper combines digital image-related technology, infrared radiation temperature measurement technology, and acoustic emission technology to carry out non-contact, real-time, non-destructive monitoring of fractured rock specimens, introduces standard deviation, and gives a detailed description of the corresponding variable field and temperature field. It accurately expresses the interrelationship between the various fields of the fractured rock specimens in the failure evolution process, and it describes the precursor reactions and abnormal points of the specimens in the failure evolution process in many aspects. Different from the previous monitoring and analysis of a single physical signal, this article uses a multi-source information monitoring method to describe the response law and damage characteristics of the fractured specimen during the destruction process. The information obtained is more accurate and comprehensive, which can not only avoid the single physical signal. The error caused by information can accurately describe the test, find the correlation between the physical signals, and increase the credibility of the test. It can also be used as a new method to study the failure evolution law of fractured rocks. However, it is far from enough to monitor and analyze multiple physical quantities. In the next step, we will integrate multiple sources of physical signals and use data fusion methods to perform fusion analysis on multiple sources of physical signals. Then, we will establish a function that considers the weight of multi-source monitoring information.

Author Contributions: Conceptualization, Q.Z. and T.Z.; methodology, Q.Z. and T.Z.; validation, Q.Z. and T.Z.; formal analysis, Q.Z. and T.Z.; investigation, Q.Z., T.Z. and Z.F.; resources, Q.Z. and T.Z.; translation, X.W.; data curation, Q.Z., T.Z. and Z.F.; writing—original draft preparation, Q.Z. and T.Z.; writing—review and editing, Q.Z. and T.Z.; visualization, Q.Z. and T.Z.; supervision, Q.Z. and T.Z.; project administration, Q.Z. and T.Z. All authors have read and agreed to the published version of the manuscript.

Funding: National Natural Science Foundation of China (NSFC) (51804008); National major scientific instrument development project (51427804); Supported by national Key RESEARCH and development Program of China (2019 YFC1904304).

Institutional Review Board Statement: Not applicable.

Informed Consent Statement: Not applicable.

Data Availability Statement: The data presented in this study are available on request from the corresponding author.

Conflicts of Interest: The authors declare no conflict of interest. The funders had no role in the design of the study; in the collection, analyses, or interpretation of data; in the writing of the manuscript, or in the decision to publish the results.

References

- Jing, L. A review of techniques, advances and outstanding issues in numerical modelling for rock mechanics and rock engineering. *Int. J. Rock Mech. Min. Sci.* **2003**, *40*, 283–353. [[CrossRef](#)]
- Park, C.H.; Bobet, A. Crack coalescence in specimens with open and closed flaws: A comparison. *Int. J. Rock Mech. Min.* **2009**, *46*, 819–829. [[CrossRef](#)]
- Zhang, K.; Li, N. Evolution law and precursor identification of fractured sandstone strain field based on digital image correlation method. *Hydrogeol. Eng. Geol.* **2021**, *48*, 150–156. [[CrossRef](#)]
- Du, Y.; Xie, M.; Jiang, Y.; Liu, W.; Liu, R.; Liu, Q. Research progress in early warning of collapse based on dynamic monitoring indicators. *J. Eng. Sci.* **2019**, *41*, 427–435. [[CrossRef](#)]
- Du, Y.; Wu, Z.; Xie, M.; Liu, R.; Chen, C. Early warning methods and experimental verification of rock mass collapse. *J. China Coal Soc.* **2019**, *44*, 3069–3075. [[CrossRef](#)]
- Li, Z.; Xu, G.; Dai, Y.; Zhao, X.; Fu, Y. Effects of foliation on deformation and failure mechanism of silty slates. *Int. J. Rock Mech. Min. Sci.* **2021**, *141*, 104703. [[CrossRef](#)]
- Zhang, G.; Li, H.; Wang, M.; Deng, S.; Wang, Z. Study on characteristics of failure strength and crack propagation of granite rocks containing a single fissure. *Chin. J. Rock Mech. Eng.* **2019**, *38*, 2760–2771. [[CrossRef](#)]
- Lou, Q.; He, X. Experimental study on infrared radiation temperature field of concrete under uniaxial compression. *Infrared Phys. Technol.* **2018**, *90*, 20–30. [[CrossRef](#)]
- Yuan, Y.; Pan, P.Z.; Zhao, S.K.; Wang, B.; Song, G.H. Research on the failure process of marble with filled cracks under uniaxial compression based on digital image correlation method. *Chin. J. Rock Mech. Eng.* **2018**, *37*, 339–351. [[CrossRef](#)]
- Shirole, D.; Hedayat, A.; Walton, G. Damage monitoring in rock specimens with pre-existing flaws by non-linear ultrasonic waves and digital image correlation. *Int. J. Rock Mech. Min. Sci.* **2021**, *142*, 104758. [[CrossRef](#)]
- Song, Y.M.; Ma, S.P.; Yang, X.B.; Wang, X. Experimental investigation on failure of rock by digital speckle correlation methods. *Chin. J. Rock Mech. Eng.* **2011**, *30*, 170–175.
- Zhang, K.; Li, N.; Chen, Y.; Liu, W. Evolution characteristics of strain field and infrared radiation temperature field during deformation and rupture process of fractured sandstone. *Rock Soil Mech.* **2020**, *41*, 95–105. [[CrossRef](#)]
- Li, C. *Application Research of Acoustic Emission Technology in Concrete Beam Failure Monitoring*; South China University of Technology: Guangzhou, China, 2018.
- Lin, Q.; Cao, P.; Wen, G.; Meng, J.; Cao, R.; Zhao, Z. Crack coalescence in rock-like specimens with two dissimilar layers and pre-existing double parallel joints under uniaxial compression. *Int. J. Rock Mech. Min. Sci.* **2021**, *139*, 104621. [[CrossRef](#)]
- Lacidogna, G.; Piana, G.; Accornero, F.; Carpinteri, A. Multi-technique damage monitoring of concrete beams: Acoustic Emission, Digital Image Correlation, Dynamic Identification. *Constr. Build. Mater.* **2020**, *242*, 118114. [[CrossRef](#)]
- Guo, K.L.; Yang, L.; Sheng, X.C.; Mei, J.; Xiang, L.B.; Zhang, B.; Yang, W.M.; Song, G.X. Fracture mechanical behavior and AE characteristics of rock-like material containing 3-D crack under hydro-mechanical coupling. *Rock Soil Mech.* **2019**, *40*, 4380–4390. [[CrossRef](#)]
- Wu, X.; Gao, X.; Zhao, K.; Liu, J.; Liu, X. Abnormality of transient infrared temperature field (ITF) in the process of rock failure. *Chin. J. Rock Mech. Eng.* **2016**, *35*, 1578–1594. [[CrossRef](#)]
- Wang, C.; Lu, Z.; Liu, L.; Chuai, X.; Lu, H. Predicting points of the infrared precursor for limestone failure under uniaxial compression. *Int. J. Rock Mech. Min. Sci.* **2016**, *88*, 34–43. [[CrossRef](#)]
- Cao, K.; Ma, L.; Zhang, D.; Lai, X.; Zhang, Z.; Khan, N.M. An experimental study of infrared radiation characteristics of sandstone in dilatancy process. *Int. J. Rock Mech. Min. Sci.* **2020**, *136*, 104503. [[CrossRef](#)]
- Shen, R.; Li, H.; Wang, E.; Chen, T.; Li, T.; Tian, H.; Hou, Z. Infrared radiation characteristics and fracture precursor information extraction of loaded sandstone samples with varying moisture contents. *Int. J. Rock Mech. Min. Sci.* **2020**, *130*, 104344. [[CrossRef](#)]
- Sun, X.; Xu, H.; He, M.; Zhang, F. Experimental investigation of the occurrence of rockburst in a rock specimen through infrared thermography and acoustic emission. *Int. J. Rock Mech. Min. Sci.* **2017**, *93*, 250–259. [[CrossRef](#)]
- Engineering behaviour of rocks. Second edition: Farmer, I London: Chapman and Hall, 1983, 208P. *Int. J. Rock Mech. Min. Sci. Geomech. Abstr.* **1984**, *21*, 123. [[CrossRef](#)]

23. Experimental fracture mechanics data for rocks and minerals: Atkinson, B.K.; Meredith, P.G. In *Fracture Mechanics of Rock*, edited by B K Atkinson P477–525. Publ London: Academic Press, 1987. *Int. J. Rock Mech. Min. Sci. Geomech. Abstr.* **1988**, *25*, A202. Available online: <https://www.sciencedirect.com/science/article/abs/pii/0148906288918669?via%3Dihub> (accessed on 4 January 2022).
24. Chen, G.; Zhang, Y.; Li, Y.; Pan, Y.; Jin, C. A Preliminary Study on the Thermal-Acoustic Precursor Information Chain of True Triaxial Loading Failure of Rocks. *Chin. J. Rock Mech. Eng.* **2021**, *40*, 1764–1776. [[CrossRef](#)]
25. Wang, S.; Zhang, Y.; Zhang, N.; Li, Z. Experimental study on acoustic emission measurement and localization of anisotropic rock mass failure process. *J. Northeast. Univ. (Nat. Sci. Ed.)* **2007**, *28*, 1033–1036.